# Eutectic growth under acoustic levitation conditions

W. J. Xie,* C. D. Cao, Y. J. Lü, and B. Wei
*Department of Applied Physics, Northwestern Polytechnical University, Xi'an 710072, People's Republic of China*
(Received 6 June 2002; published 10 December 2002)

Samples of Pb-Sn eutectic alloy with a high density of $8.5\times10^3$ kg/m$^3$ are levitated with a single-axis acoustic levitator, and containerlessly melted and then solidified in argon atmosphere. High undercoolings up to 38 K are obtained, which results in a microstructural transition of ''lamellas–broken lamellas–dendrites.'' This transition is further investigated in the light of the coupled zone for eutectic growth and the effects of ultrasound. The breaking of regular eutectic lamellas and suppression of gravity-induced macrosegregation of (Pb) and (Sn) dendrites are explained by the complicated internal flow inside the levitated drop, which is jointly induced by the shape oscillation, bulk vibration and rotation of the levitated drop. The ultrasonic field is also found to drive forced surface vibration, which subsequently excites capillary ripples and catalyzes nucleation on the sample surface.

DOI: 10.1103/PhysRevE.66.061601 PACS number(s): 81.30.Fb, 64.70.Dv, 43.35.+d

## I. INTRODUCTION

The investigation of eutectic growth is of interest in both technological applications and fundamental studies as an example of spontaneous pattern formation in nature [1–10]. Eutectic growth involves the interacting nucleation and cooperative growth of two or more solid product phases within one liquid parent phase. Since the pioneering work by Jackson and Hunt [11], theoretical descriptions of eutectic growth have been extensively studied on the basis of the coupled diffusion field ahead of growth front and the marginal stability of the liquid-solid interface [12]. The resultant microstructure is strongly dependent on heat, solute, and mass transportation in the liquid phase ahead of liquid-solid interface, which can be controlled by cooling rate or undercooling prior to solidification. In practice, the natural or forced convection is also an important mechanism to govern the heat and solute transportation in a complicated way. Dendrites and eutectics are two of the most typical morphologies in solidification processes. During the solidification of a eutectic system, there also exists competitive growth between eutectics and dendrites. The undercoolings, which lead to an entirely eutectic growth for a composition range, make up what is known as the coupled zone of eutectics [12].

Containerless processing eliminates the heterogeneous nucleation catalyzed by the contact between the melt surface and container walls [13–16]. This allows achievement of large undercoolings and rapid solidification far from thermodynamic equilibrium. As a result, a metastable, amorphous, or solid solubility extended microstructure is possible to form [15]. For binary eutectic alloys, containerless processing techniques provide chances to undercool the melts far below their equilibrium freezing temperatures, which results in rapid eutectic growth and ''lamellar-anomalous'' microstructural transition when the undercooling exceeds a critical value [16].

The containerless state of an object can be achieved by levitation techniques employing acoustic, aerodynamic, magnetic, electromagnetic, or electrostatic forces [17–22]. Electromagnetic field may have the strongest levitation ability but the sample must be conductive and with a high melting temperature to avoid being overheated to evaporate by the eddy current inside the sample. For dielectric substances or those metallic substances with a low melting temperature, it is proper to employ acoustic levitation because there are no limits to the electric and magnetic properties of the sample, and no coupling with strong heating effect like that in electromagnetic levitation.

So far, containerless melting and solidification of low-density organic materials has been performed with a single-axis acoustic levitation technique [23–26]. Since the force produced by acoustic field is comparatively weak, it is difficult to extend this technique to high-density metallic substances. We have managed to enhance the levitation force and stability of a single-axis acoustic levitator remarkably by optimizing its geometric parameters [27,28]. We also managed to control the various instabilities caused by heating and cooling processes during acoustic levitation. These enable us to melt and solidify the acoustically levitated samples of Pb-Sn eutectic alloy which has a high density of $8.5\times10^3$ kg/m$^3$.

In the studies of undercooling and solidification of acoustically levitated substances, there is a strong concern that ultrasound may influence the undercooling and solidification processes. The work of Ohsaka *et al.* [24] has shown that ultrasound occasionally prematurely terminates undercooling of the levitated succinonitrile drops by initiating nucleation that was explained by the cavitation effect. Since a liquid drop levitated in acoustic field often experiences complicated vibration, oscillation and rotation, the diffusion field for heat and solute transportation may be affected remarkably by the induced internal flow inside the drop. In this paper, we extend the application of the single-axis acoustic levitation to the containerless melting and solidification of Pb-Sn eutectic alloy. The characteristics of eutectic growth under acoustic levitation conditions, including nucleation and crystal growth, are discussed in terms of a containerless state and complicated movement of the levitated samples inherently related to ultrasonic field.

*Corresponding author. Email address: lmss@nwpu.edu.cn

 

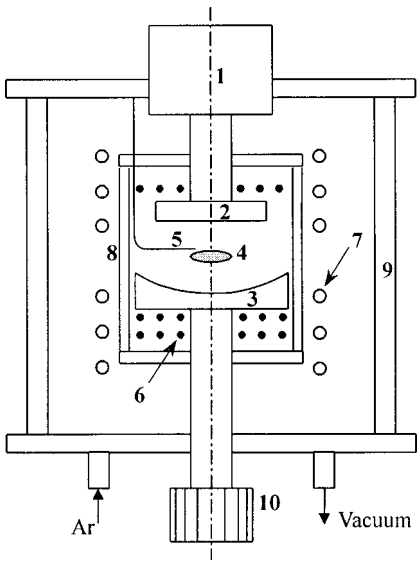


FIG. 1. Schematic of experimental setup: 1, transducer; 2, emitter; 3, reflector; 4, sample; 5, thermocouple; 6, resistance coils; 7, cooling tube; 8, Glass tube: 9, vacuum chamber; and 10, adjusting handle.

## II. EXPERIMENTAL PROCEDURE

Figure 1 shows schematically the main parts of the single-axis acoustic levitation system capable of performing heating and cooling of the levitated samples. The driving component is a magnetostrictive transducer working at a frequency of 16.7 kHz. The ultrasonic vibration produced by the transducer is amplified and introduced into the emitter head by a horn that connects the emitter with the transducer. A reflector with a spherically concave surface is placed below the emitter to produce the necessary strong standing wave for levitation of the sample against gravity. The sample is levitated at the first resonant state, and is heated by two resistance coils placed above the vibrating head and below the reflector, respectively. In order to avoid violent convection of the gas medium during heating and cooling, the levitation system is enclosed by a glass tube without hermetic sealing. The cooling of the sample is conducted indirectly by water flowing inside a copper coil around the levitator. The levitator along with the heating and cooling units is enclosed inside a vacuum chamber made of transparent polymethyl methacrylate, which is evacuated to 0.1 Pa and then back-filled with 1 atm argon gas. The temperature is measured by a NiCr-NiSi thermocouple. The tip of this thermocouple is placed above the levitated sample with a separation of about 1 mm.

A spherical sample acoustically levitated in a terrestrial condition always experiences large shape deformation after melting, especially when the density of the sample is higher to require more intense acoustic field. This deformation often arouses unexpected violent instability. To reduce this deformation degree and make the melting process accomplish smoothly, the solid sample to be levitated is shaped into a disk of 4 mm diam and 1.2 mm thickness which is near the final equilibrium shape of the melted liquid drop. The sample is placed on the center of the reflecting surface at first and heated to a temperature around 373 K, before the ultrasonic transducer is turned on. Then the sample is levitated and controlled in a stable state by adjusting the reflector-emitter interval. During the following heating and cooling processes, the variation of argon wavelength resulting from temperature change leads to serious deterioration of the resonant state of the acoustic field. Therefore, careful adjusting of the reflector-emitter distance has to be performed according to the temperature variations to keep resonance inside the glass tube during the remainder of the experiment. The samples are usually heated to a temperature 30–40 K above the eutectic temperature, and then subjected to cooling. The solidified samples are sectioned, mounted in epoxy resin, and polished for metallographic investigation. The microstructures are analyzed by an XJG-05 optical microscope, a Regaku/Dmax III-C x-ray diffractometer and a HITACHI S2700 scanning electron microscope.

## III. PHYSICAL CONDITIONS OF ACOUSTIC LEVITATION WITH HEATING AND COOLING

During the heating and cooling processes of acoustically levitated samples, there are great changes in the density and sound speed of the gas medium, which strongly affects the levitation force and stability and often leads to a failure of the experiment. The facts lie in two aspects: either the sound intensity becomes too small to counteract the gravity, or it becomes too large to keep the stability and integration of the liquid drop. In the former case, the sample falls down and attaches to the reflector; whereas in the latter case, the liquid drop is drastically flattened and then buckled or atomized. The buckling of the liquid drop ultimately leads to the fall or disintegration of that drop. The physical conditions that are strongly affected by heating and cooling process include: (1) The wavelength dependent resonance of the acoustic field; (2) the density and wavelength dependent acoustic levitation force; and (3) the density and wavelength dependent threshold pressures to entrap a sample and to initiate drop instability.

In the present experiment, in order to avoid the violent convection induced by inhomogeneous temperature field, the heating and cooling are performed in a very slow rate. Therefore, the gas medium can be regarded as in a quasistatic state of thermodynamic equilibrium. Moreover, the acoustic vibration and the by-produced acoustic streaming are beneficial to promote temperature homogeneity between the heating source and the levitation region. Thus, to have a brief insight into the physical conditions of the single-axis acoustic levitation with heating and cooling, we will not discuss the temperature gradient here. Considering argon as an ideal gas, and the atmosphere pressure inside the vacuum chamber maintaining at unit atm, the density and sound speed of argon vary with temperature in the forms of $\rho=\rho_0(273/T)$, and $c=c_0(T/273)^{1/2}$, respectively. Here, $\rho_0=1.78$ kg/m, and $c_0=319$ m/s are the density and sound speed at $T=273$ K. The Pb-Sn eutectic alloy has an expansion coefficient much smaller than that of argon, and its density and volume variation with temperature change are neglected.

For a plane standing wave approximation, the resonant condition of the acoustic field is described as

$$H = 0.5\sqrt{T/273}\lambda_0, \tag{1}$$

where, $H$ is the interval between the emitter and the reflector and $\lambda_0 = 19.1\times10^{-3}$ m is the wavelength of argon at 273 K.

According to the classic formula of acoustic radiation force with the plane standing wave approximation [29,30], the minimum sound pressure to entrap a sample in 1 g condition can be expressed as

$$p_m = \left(\frac{4\rho_s\rho_0 g c_0^3}{5\pi f_0}\right)^{1/2}\left(\frac{T}{273}\right)^{1/4}. \tag{2}$$

where, $\rho_s = 8.5\times10^3$ kg/m is the density of the Pb-Sn eutectic alloy, $f_0 = 16.7$ kHz is the frequency of the acoustic field, and $g = 9.8$ m/s$^2$ is the gravitational acceleration.

When the sound pressure exceeds a critical threshold, the levitated liquid drop will become drastically flattened and unstable, and disintegration or buckling may occur to it. This threshold pressure can be evaluated as [31]

$$p_M = c_0\left(\frac{3.4\sigma\rho_0}{R_S}\right)^{1/2}, \tag{3}$$

where, $\sigma = 0.44-(T-823)\times0.13\times10^{-3}$ N/m is the surface tension of the liquid, and $R_s = 1.58\times10^{-3}$ m is the equivalent radius of the drop in a spherical shape. It is obvious that the actual sound pressure amplitude $\rho_0$ should be maintained in the scope of $p_m < p_0 < p_M$ during the stage when the sample is in the liquid state.

As to the acoustic levitation system depicted in Fig. 1, where a spherically concave reflecting surface is applied, the acoustic field between the reflector and the emitter is actually not a plane standing wave. Therefore, the resonant condition, the minimum entrapping pressure and the instability threshold pressure have a deviation from that described in Eqs. (1)–(3). We have developed a two-cylinder model to describe the single-axis acoustic levitation system [27,28]. This model shows that the resonant state and the levitation force and stability are strongly dependent on the geometric parameters of the levitator with reference to wavelength. In the present experiment, the geometric parameters of the levitator are fixed, whereas the wavelength of argon varies with heating and cooling performance. Consequently, there appears a new factor to influence the physical conditions of acoustic levitation that depends upon the variation of the ratios of geometric parameters to wavelength, now aroused by temperature change.

Based on this model, the resonant condition corresponding to the present experiment is calculated, as shown in Fig. 2. The resonant peak location has a weak dependence on temperature. This dependence can be linearly fitted as $H/\lambda = 0.56+7.827\times10^{-5}$ T, in the temperature range of $373 < T < 503$ K. Therefore, the present resonant condition can be written as

$$H = (0.56+7.827\times10^{-5}T)\sqrt{T/273}\lambda_0. \tag{4}$$

Equation (4) indicates that during the heating and cooling processes, the reflector-emitter interval should be adjusted carefully according to the temperature variation to keep the resonance of the acoustic field. For a typical heating process, the interval begins with $H = 13.15$ mm at $T = 373$ K, and ends with $H = 15.54$ mm at $T = 503$ K. Practically, it is hard to follow Eq. (4) in the experiment by manual operation. Instead, we always make the reflector-emitter interval slightly larger than the resonant condition of Eq. (4). Thus, when the temperature increases, the resonant condition is strengthened and levitation force is enhanced, which lifts the sample towards the thermocouple tip above it. Once this takes place, we adjust the interval slightly longer, to weaken the resonant condition and keep a certain separation between the thermocouple tip and the sample. By this means, the acoustic field is kept in a state very near the resonant condition. Similarly, when the temperature decreases, the reversed operation is conducted.

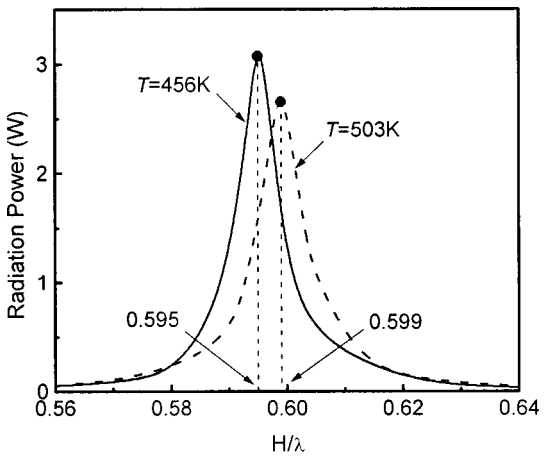


FIG. 2. Resonance of the acoustic field at different temperatures. Here $H$ is the reflector-emitter interval, and $\lambda$ is the wavelength.

The total force exerted on the sample is the sum of the acoustic radiation force, the gravitational force, and the buoyancy (the buoyancy is negligible in the present case). The characteristics of the total force can be depicted by the potential energy $U$ (defined as in Ref. [32]). Figure 3 shows the distribution of the sound pressure $p$ and the time-

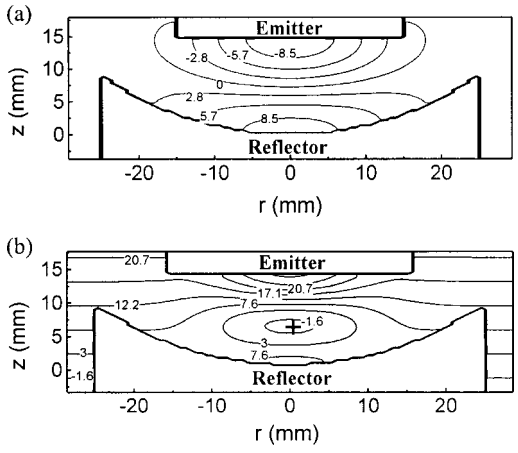


FIG. 3. Contours of (a) sound pressure $p$ (unit: $\times10^3$ Pa), and (b) force potential $U$ (unit: $\times10^{-6}$ Nm) at 456 K. The symbol "+" denotes potential minimum where the sample is located.

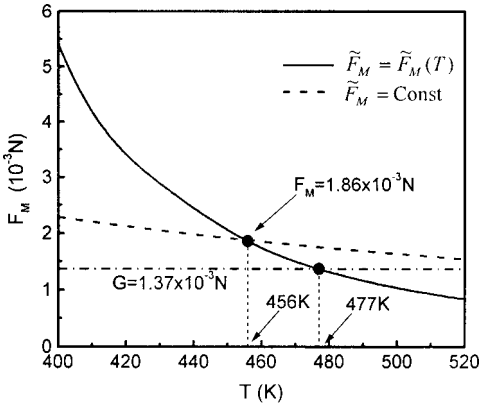


FIG. 4. Temperature dependence of the maximum levitation force. Here, $\nu_0 = 0.34$ m/s.

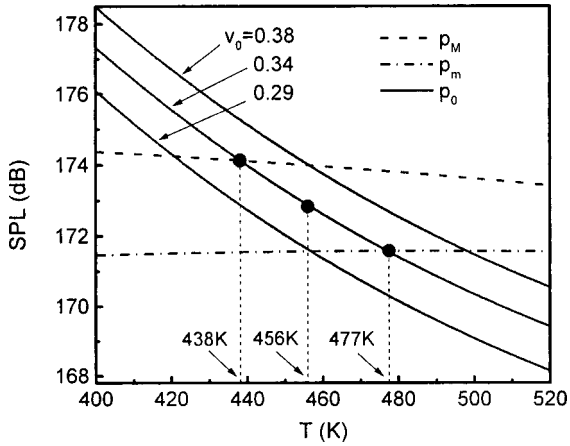


FIG. 5. Temperature dependence of the sound pressure level at given vibration amplitudes of the emitter. Here, $p_m$ is the minimum sound pressure to entrap a sample, and $p_M$ is the threshold pressure beyond which disintegration or buckling may occur to the levitated drop.

averaged potential $U$ for the total force at $T = 456$ K. It is visible that the acoustic field between the reflector and emitter is no longer a plane standing wave and there exists a pressure gradient in the horizontal directions, which can also provide radial restoring force. It can been seen that at the first resonant mode, there is only one potential well to entrap the sample, and the vertical position is shifted downward because of the gravitational field. As defined in our previous work [27,28], the maximum levitation force around a potential well can be expressed by

$$F_M = (2\pi)^2 \frac{f\rho_0 R_S^3 \nu_0^2}{c_0} \left(\frac{273}{T}\right)^{3/2} \widetilde{F}_M, \tag{5}$$

where $\nu_0$ is the vibration amplitude of the emitter surface, $f$ is the vibration frequency, and $\widetilde{F}_M$ is the dimensionless maximum levitation force that strongly depends on the geometric parameters with reference to wavelength. Since the wavelength λ is a function of temperature, $\widetilde{F}_M$ is also dependent on temperature. Figure 4 shows the temperature dependence of the maximum levitation force, which indicates that in the heating process, the maximum levitation force has a quick decline as the temperature increases. This decline is attributed mainly to the decrease of $\widetilde{F}_M(T)$. Therefore, to guarantee that $F_M$ is larger than the weight of the sample and the sound pressure is below the threshold for drop instability, the vibration amplitude of the emitter should be adjusted appropriately in the heating and cooling processes.

Considering that the acoustic field is no longer a plane standing wave, Eqs. (2) and (3) can be rewritten as

$$p_m = \alpha(T) \left(\frac{\rho_s \rho_0 g c_0^3}{3\pi f}\right)^{1/2} \left(\frac{T}{273}\right)^{1/4}, \tag{6}$$

$$p_M = \beta(T) c_0 \left(\frac{3.4\sigma\rho_0}{R_S}\right)^{1/2}, \tag{7}$$

where, $\alpha(T) = 1.595 + 1.239\times10^{-3}T - 2.192\times10^{-6}T^2$ and $\beta(T) = 0.997 + 9.156\times10^{-4}T - 1.858\times10^{-6}T^2$ are two coefficients fitted by the calculated data based on our numerical model. Figure 5 shows the variation of $p_m$ and $p_M$ as a function of temperature, which gives a minimum pressure of 171.6 dB and a maximum pressure of 174.0 dB for the stable levitation of Pb-Sn eutectic alloy at the melting point. When the temperature increases, this range is narrowed, which means that the higher the temperature is, the more difficult to control the liquid drop within a stable pressure range. Figure 5 also shows the actual sound pressure at a resonant state as a function of the temperature at given vibration intensities of the emitter. At a fixed vibration amplitude $\nu_0 = 0.34$ m/s, if the temperature increases above 477 K or decreases below 438 K, the liquid drop will either fall down or be chopped by the acoustic field. Since the pressure is proportional to the vibration amplitude of the emitter surface, the input power into the transducer should also be adjusted appropriately to guarantee $p_m < p_0 < p_M$. In fact, we can maintain the emitter intensity at a comparatively high level to ensure sufficient levitation force, and at the same time slightly weaken the resonant condition to avoid the sound intensity being too large. This method proves to be successful in our experiment.

## IV. RESULTS AND DISCUSSIONS

### A. Eutectic growth and resultant microstructures

The location of the Pb-Sn eutectic alloy in the phase diagram is shown in Fig. 6, which has a composition of 61.9 wt % of Sn, and an equilibrium eutectic temperature of 456 K. The density of this alloy is $8.5\times10^3$ kg/m$^3$ at room temperature. Figure 7 shows the typical cooling curves of the Pb-Sn eutectic alloy in the experiment. Because of the slow cooling rate (5–8 K/min), the temperature measured by the nearby thermocouple is rather accurate before and late after the recalescence [26]. During and soon after the recalescence, the abrupt release of heat from the sample will lead to a temperature difference of about 3–5 K between the sample and the thermocouple. This heat release along with the state change of the sample from liquid to solid makes the sample vibrate and rotate more violently, which can be reflected by the quivers in the cooling curves. The beginning of the abrupt temperature rise (recalescence) allows us to determine

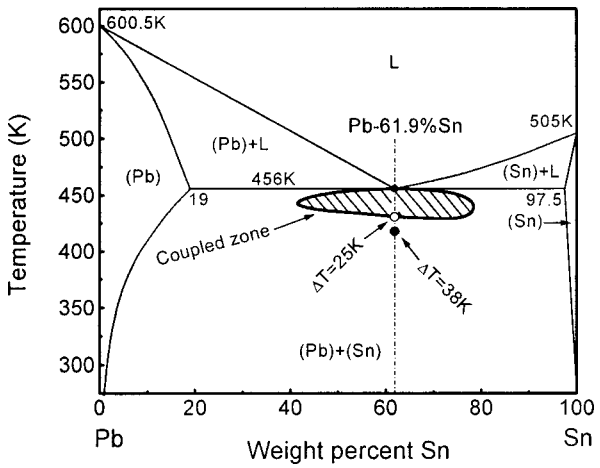


FIG. 6. Binary phase diagram of Pb-Sn eutectic system and calculated coupled zone for eutectic growth.

the undercoolings. In our experiment, a maximum undercooling of 38 K ($0.083T_E$) has been obtained. The solidification process of highly undercooled melts after nucleation involves two distinct stages: (1) the initial rapid solidification accompanying recalescence, corresponding to the temperature rise in the cooling curves; and (2) the following slow solidification after recalescence, corresponding to the thermal plateau. For small undercoolings, there is an obvious thermal plateau after the recalescence event. As shown in Fig. 7, the duration of the thermal plateau for $\Delta T = 17$ K is 40 s. When the undercooling increases, the duration time shortens, and when undercooling exceeds 31 K, the plateau becomes unclear. This behavior shows the characteristics of the solidification from highly undercooled melts.

The microstructure evolution of Pb-Sn eutectic alloy with the increase of undercooling is shown in Fig. 8. Under static and near-equilibrium conditions, Pb-Sn eutectic grows in the form of alternating lamellas of (Pb) and (Sn) phases, as shown in Fig. 8(a). This lamellar structure is observed in samples undercooled by up to 17 K in our experiment. When the undercooling exceeds 31 K, the microstructure is characterized by dendrites composed of both lead-rich and tin-

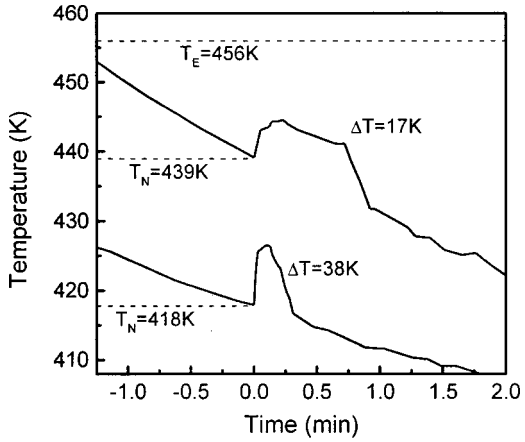


FIG. 7. Cooling curves and recalescence of acoustically levitated Pb-Sn eutectic alloy.

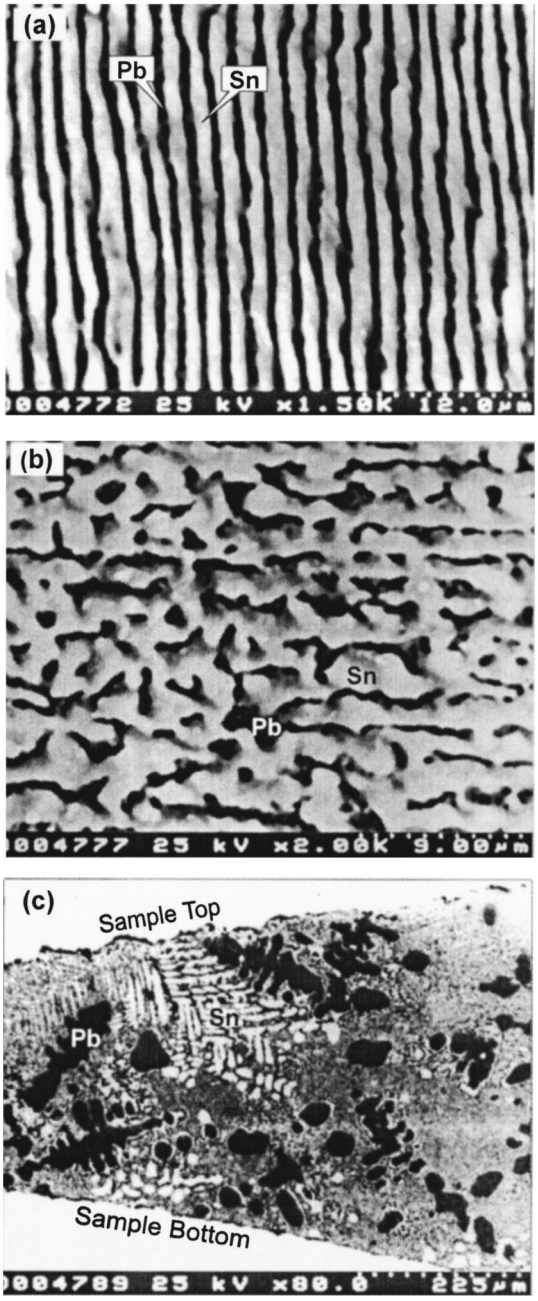


FIG. 8. Microstructural transition of Pb-Sn eutectic alloy: (a) under static condition, (b) acoustically levitated, $\Delta T = 17$ K, and (c) acoustically levitated, $\Delta T = 38$ K.

reach phases, as shown in Fig. 8(c). This ''eutectic-dendrites'' transition can be explained by a eutectic coupled zone, which is defined as the range of compositions and interface temperatures in which the eutectic growth leads the growth front. The boundary of the coupled zone can be calculated by comparing the growth velocities of the eutectic with that of the dendrites possessing the same composition, on the basis of eutectic growth theory by Trivedi, Magnin, and Kurz [33] and the dendritic growth theory by Lipton, Kurz, and Trivedi [34]. For dendritic growth, the growth velocity $V$, dendrite tip radius $R$, and undercooling $\Delta T$ satisfy the following equations [34]:

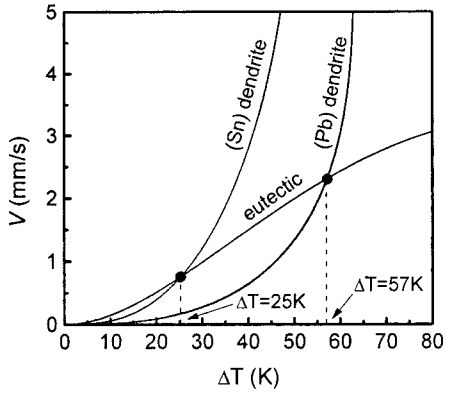


FIG. 9. Calculated crystal growth velocities in undercooled Pb-Sn eutectic alloy.

$$\Delta T=\Delta T_c+\Delta T_t+\Delta T_r+\Delta T_k, \tag{8}$$

$$R=\frac{\Gamma/\sigma^*}{\theta_t P_t \xi_t-2\theta_c P_c \xi_c}, \tag{9}$$

where $\Delta T_c$, $\Delta T_t$, $\Delta T_r$, and $\Delta T_k$ are the partial undercoolings due to solute diffusion, heat flow, dendrite tip curvature, and nonequilibrium kinetics, respectively, $\Gamma$ is the Gibbs-Thomson coefficient, $\sigma^*=1/(4\pi^2)$ is the stability constant, $\theta_t$ and $\theta_c$ are the unit thermal and solute undercoolings, $P_t$ and $P_c$ are the thermal and solute Peclet numbers, and $\xi_t$ and $\xi_c$ are the thermal and solute stability functions, respectively.

For eutectic growth, the inter-relationship between the growth velocity $V$, interlamellar spacing $\lambda$, and undercooling $\Delta T$ is described by the following two equations [33]:

$$\lambda^2 V=a^L/Q^L \tag{10}$$

$$\lambda\Delta T=ma^L\left[1+\frac{P}{P+\lambda(\partial P/\partial\lambda)}\right]. \tag{11}$$

Here $a^L$ and $m$ are two constants determined by the volume fraction, capillarity constant, and liquidus slope of (Pb) and (Sn) phases. $Q^L$ and $P$ are two functions with the diffusion coefficient, solute partition coefficient, and the solute Peclet number at the liquid-solid interface as their arguments. The details of these definitions can be found in Ref. [33].

The calculated eutectic coupled zone is superimposed on the phase diagram in Fig. 6. It predicts broad composition (43–78 wt % Sn) and undercooling (0–25 K) ranges within which the lamellar eutectic growth manner is dominant. Whereas, beneath the eutectic coupled zone, (Pb) or (Sn) dendrite is preferential to grow. In this case, an anomalous eutectic microstructure may also appear in practice [16]. The work of deGroh and Laxmannan [35] on Pb-Sn eutectic alloy shows that (Pb) dendrites nucleate and grow first, making the remaining liquid richer in tin and thus promoting subsequent growth of tin-rich off eutectics or the growth of tin-rich dendrites. The primary (Pb) phase is not a potent nucleant for eutectic growth; on the contrary, it is the secondary (Sn) phase that nucleates the eutectic growth [35]. Figure 9 shows the comparison of the calculated growth velocities among the eutectic, (Pb) and (Sn) dendrites, which indicates that when the undercooling is larger than 25 K, the secondary (Sn) phase will grow in a dendritic manner rather than grow by cooperating with the (Pb) phase in a lamellar eutectic manner. This agrees with observed microstructures as shown in Figs. 8(b) and 8(c). The physical parameters used for the above calculation are listed in Table I.

TABLE I. Physical parameters used for the calculation of eutectic growth and dendritic growth in Pb-Sn eutectic alloy.

| | |
|---|---|
| Eutectic composition $C_E$ (wt. %) | 61.9 |
| Eutectic temperature $T_E$ (K) | 456 |
| Volume fraction $f$ of (Pb) phase | 0.374 |
| Equilibrium partition coefficient $k_e$ of Pb phase | 0.307 |
| Equilibrium partition coefficient $k_e$ of Sn phase | 0.066 |
| Liquidus slope $m_\alpha$ of (Pb) phase $[K/(\text{wt. \%})]$ | 2.27 |
| Liquidus slope $m_\beta$ of (Sn) phase $[K/(\text{wt. \%})]$ | 0.86 |
| Capillary constant $\alpha_\alpha^L$ of (Pb) phase (m K) | $4.5\times10^{-7}$ |
| Capillary constant $\alpha_\beta^L$ of (Sn) phase (m K) | $7.5\times10^{-7}$ |
| Characteristic diffusion length $a_0$ (m) | $5\times10^{-10}$ |
| Prefactor of diffusion coefficient $D_0$ ($m^2$ s) | $3.23\times10^{-8}$ |
| Activation energy $Q$ for solute diffusion (J/mol) | 19600 |
| Heat of fusion $\Delta H$ (J/mol) | 7280 |
| Specific heat of alloy melt $C_{pL}$ [J/(mol K)] | 30.63 |
| Liquid-solid interface energy $\sigma_\alpha^L$ of (Pb) phase ($J/m^2$) | $4.3\times10^{-2}$ |
| Liquid-solid interface energy $\sigma_\beta^L$ of (Sn) phase ($J/m^2$) | $5.8\times10^{-2}$ |
| Thermal diffusion coefficient $\alpha_L$ ($m^2$ s) | $1.5\times10^{-5}$ |

It has been reported that in high undercooling conditions, metastable phases may appear in the Pb-Sn system [36]. The samples with different undercoolings are analyzed by x-ray diffraction (XRD). No metastable phase is found in the undercooling range of 0–38 K in our experiment. The XRD pattern of Fig. 10 indicates that the microstructures are composed of (Pb) and ($\beta$-Sn) phases.

### B. Breaking of eutectic lamellas and suppression of gravity-induced macrosegregation

When levitated by ultrasound in a contact-free state, some new characteristics of the solidified Pb-Sn eutectic alloy are also found. At a small undercooling of 17 K that lies inside

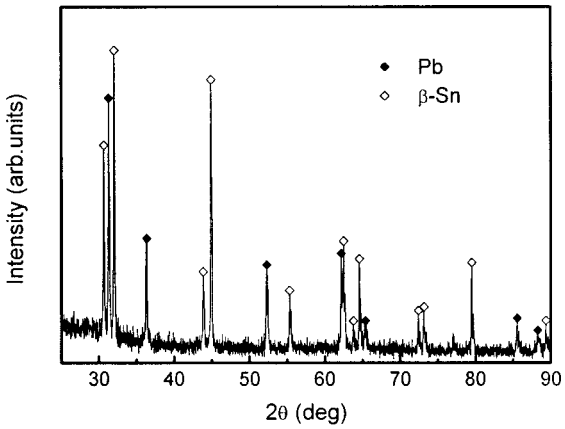


FIG. 10. X-ray diffraction patterns of Pb-Sn eutectic alloy.

the coupled zone [see Fig. 8(b)], a microstructure consisting of broken and distorted lamellas has been observed in addition to some fractions of remnant regular lamellas. These broken lamellas are quite different from those regular lamellar structures predicted by the coupled zone in static conditions. If the undercooling goes beyond the coupled zone, both the (Pb) and (Sn) phases nucleate and grow into dendrites. Due to the large density difference between lead and tin ($\rho_{\mathrm{Pb}}=11.4\times10^3$ and $\rho_{\mathrm{Sn}}=7.3\times10^3$ kg/m$^3$), (Pb) dendrites generally sink downward and (Sn) dendrites float upward, which results in serious gravity-induced macrosegregation in the common terrestrial condition [35]. It is interesting in Fig. 8(c) that (Pb) dendrites have also appeared in the top part of the acoustically levitated sample undercooled by 38 K, and the gravity-induced macrosegregation is effectively suppressed. These characteristics of solidification are probably caused by the ultrasonic vibration, the nonuniform radiation force, and the complicated fluid flow inside the sample, rather than the containerless state.

When a liquid drop is levitated in an acoustic field, the influence of the penetrated acoustic wave inside the drop is negligible, since the liquid alloy has an acoustic impedance of $1.7\times10$ Ns/m$^3$, much larger than that of argon, $4.4\times10^2$ Ns/m$^3$, leading to penetration in the order around $10^{-5}$ of the acoustic intensity into the liquid alloy. Nevertheless, the second-order acoustic pressure and acoustic streaming intervening with the drop surface can induce complicated shape oscillation, bulk vibration, and rotation, which drive internal flow inside the liquid. Furthermore, the first-order acoustic pressure can also interact with the drop surface within a thin layer to arouse forced surface vibration [37,38] and acoustic cavitation [24].

For a near spherical inviscid liquid drop, the frequency of small oscillation is expressed by the Rayleigh relationship [39],

$$f_n^2=\frac{n(n+2)(n-1)\sigma}{4\pi^2\rho_s R_S^3}, \tag{12}$$

where $n$ is the resonant number, $\sigma$ is the surface tension, and $\rho_s$ and $R_S$ are the density and equilibrium radius of the drop. Considering the Pb-Sn eutectic sample melt ($\sigma=0.49$ N/m) with a typical mass of 0.14 g, and the typical resonant mode $n=2$, the oscillation frequency is 54.5 Hz. Although the viscosity and large deformation of the drop are not negligible in this case, they do not change the frequency too much. The shape oscillation of the drop levitated in the acoustic field is characterized by alternating expanding and contracting of the equator and polar, driving internal flow between the equator and polars inside the drop. In a steady acoustic field, this oscillation will soon be damped out due to the viscosity of the drop. But in this experiment, the acoustic field is always under adjustment, which inevitably excites shape oscillation.

Translational vibration of the drop exists in both vertical and horizontal directions. Simplifying the acoustic field as a plane standing wave, the acoustic radiation force [29,30] exerted on the sample is $F=(5/6)\pi R_S^3 k\rho_f \nu_A^2 \sin(2kz)$. Here, $R_S$ is the equivalent radius of the sample in spherical shape, $\rho_f$ is the density of the medium gas, $k$ is the wave number, and $\nu_A$ is the amplitude of the particle velocity of the acoustic field. If the sound intensity is sufficiently large, the sample will be located very near the pressure nodes of the acoustic field, where $F$ is characterized by restoring force. Therefore, the frequency of the drop vibration in the vertical direction is

$$f_\nu=\frac{p_0 f_0}{2c^2}\sqrt{\frac{5}{\rho_f\rho_s}}, \tag{13}$$

where $f_0$ is the frequency of the acoustic field, $p_0$ is the pressure amplitude, $c$ is the speed of sound, and $\rho_s$ is the density of the sample. Given SPL$=172$ dB ($p_0=1.13\times10^4$ Pa), and the experimental parameters (at 456 K) $c=412$ m/s, $f=16.7$ kHz, $\rho_f=1.07$ kg/m$^3$, $\rho_s=8.5\times10^3$ kg/m$^3$, the value of $f_\nu$ becomes 13 Hz, much lower than the acoustic frequency. During the experiment, the amplitude of the drop vibration is kept under control (not larger than 0.5 mm) by careful adjustment of the reflector-emitter distance when temperature varies. However, when the recalescence event takes place, it is difficult to control this fluctuation because of abrupt temperature rise. In this case, the fluctuating amplitude may jump upto 1–2 mm. The large amplitude and low frequency vibration of the drop will arouse violent convection inside the liquid part of the sample.

Though the acoustic wave inside the drop is negligible, the drop surface is forced to vibrate by the first-order pressure at a frequency the same as the acoustic field [38,40]. Due to the high sound intensity, the drop is usually drastically flattened, and can be considered as a membrane. The vibration of the membrane is a forced one because the acoustic frequency is much higher than that of the ''drumhead'' mode of the membrane [38]. The velocity of this vibration takes the form of $\nu=\mathrm{Re}[\nu_1\exp(-j\omega t)]$, with

$$\nu_1=\frac{2kR\rho_0\cos kZ}{i\omega\rho_s\pi h(r)}\left[1-\frac{r^2}{R^2}\right]^{1/2}, \tag{14}$$

where $R$ is the radius of the membrane disk, $r$ is the radial position on its surface, $Z$ is the distance of the disk below the pressure node from which it is levitated, $\omega=2\pi f_0$ is the angular frequency, and $h$ is the half-thickness of the membrane. According to Eq. (3), for a typical flattened drop, $R/h\sim5$, the velocity amplitude at the center of the membrane becomes $\nu\sim10^{-2}$ m/s and the corresponding displacement is $\sim10^{-7}$ m only. This vibration amplitude is too weak to induce internal flow inside the drop. However, because of the high frequency of this vibration, the corresponding acceleration is large enough ($\sim10^3$ m/s$^2\sim10^2$ g) to excite capillary waves on the drop surface.

For the single-axis acoustic levitation, the rotation of the drop around the symmetry axis is uncontrolled, which produces centrifugal force to flatten the drop further [41]. When the rotation is accelerated or decelerated by random external torque, there will appear laminar flow between the outer layer and the inner layer of the drop, due to the inertia difference. A summary of the characteristic parameters for the above movements has been listed in Table II.

The application of vibration during solidification has been extensively studied in the past 3 decades. The striking effects

TABLE II. Estimated movement parameters of the acoustically levitated Pb-Sn eutectic alloy drops.

| Movements | Frequency (Hz) | Amplitude ($\mu$m) |
|---|---|---|
| Shape oscillation | 54.5 | $\sim 10^2$ |
| Vertical vibration | 13 | $10^2 \sim 10^3$ |
| Surface vibration | 16700 | $\sim 10^4$ |
| Rotation | 0–10 | |
| Capillary waves | 8350 | $\sim 10^0$ |

include refining grain size, degassing the melt, suppressing the shrink pipe, and reducing segregation [42–46]. The corresponding mechanisms are usually interpreted in two aspects. One is the acoustic cavitation effect and the other is the acoustically induced bulk flow inside the melts. Since the direct action of the intense ultrasound only plays in a thin layer of the drop surface when levitated acoustically, the characteristics of broken lamellas and suppression of macrosegregation must be attributed to the internal flow of the melt. As analyzed above, the flow inside an acoustically levitated drop is a much complicated one, jointly initiated from the shape oscillation, translational vibration and rotation, with a wide range of amplitudes and frequencies. The roles of vibration-induced flow inside the melt have been found to change the concentration and temperature gradient ahead of the liquid-solid interface [43,44], and also to counteract the buoyancy- and/or thermocapillary-driven convection [45,46]. The latter role can explain the reduction of the gravity-induced macrosegregation of (Pb) and (Sn) dendrites. Since the movement of the acoustically levitated drop is a combination of oscillation, vibration, and rotation, it is natural to assume another role of this movement, i.e., stirring the liquid part of the sample, which may be responsible for the breaking of the eutectic lamellas.

### C. Capillary wave related surface nucleation

The complexity of the movement of an acoustically levitated drop can also be manifested by the capillary wave appearing on the surface of the drop. An effect of the nonuniform acoustic radiation force is that it compresses the levitated liquid drop into a pancakelike shape [38]. Moreover, it often ''hits'' into a dimple at the central part of the top or bottom surface of the levitated sample, where the ultrasound and energy are usually focused [38]. A clue that this nonuniform radiation force also influences Pb-Sn eutectic solidification is found at the surface of such a dimple, as shown in Fig. 11(a), which looks like the spreading ripples on a disturbed water surface. The ripples were believed to be the capillary waves generated by the parametric instability excited by a low-amplitude surface vibration [37,38]. The frequency of the capillary wave is half that of the acoustic vibration [37]. And the capillary wavelength $\lambda_c$ is given by the classic Faraday dispersion relation [37]

$$\omega_c^2 = \sigma k_c^3 / \rho_s , \tag{15}$$

where $\omega_c$ is the angular frequency, $k_c$ is the wave number $2\pi/\lambda_c$, and $\sigma$ is the surface tension. This relationship gives

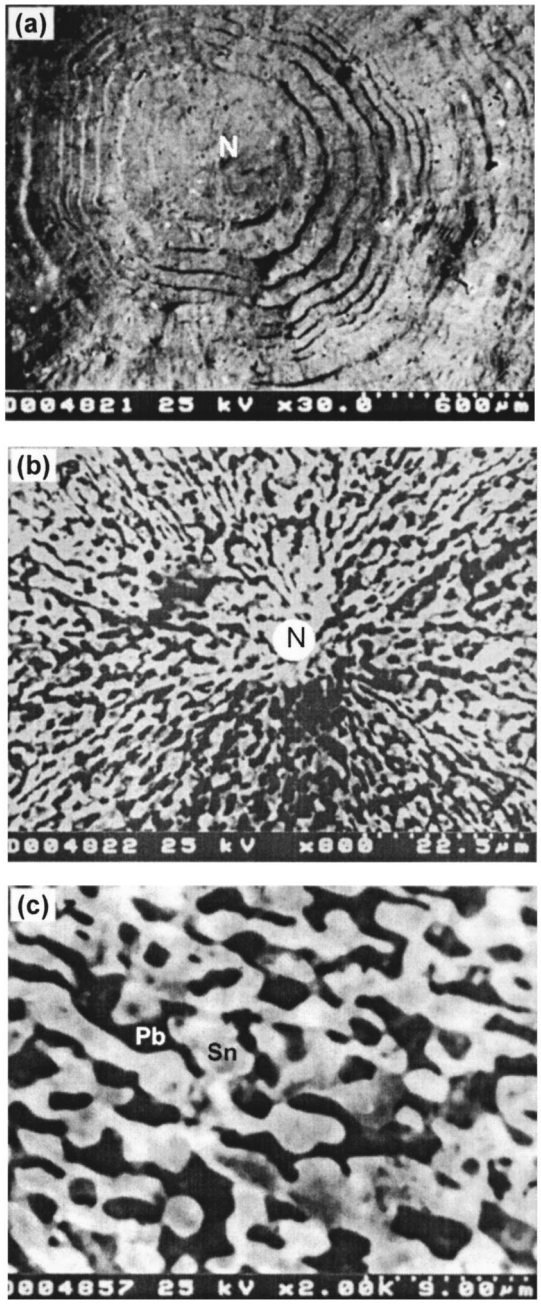


FIG. 11. (a) ''Spreading ripples'' on the top surface of a pancakelike sample undercooled by 15 K; (b) enlargement of the central part of the ripples shown in (a), which is characterized by broken and distorted lamellar eutectics radiating from the ripples center; (c) enlargement of the broken and distorted lamellar eutectics shown in (b). Here *N* denotes the center of ripples.

a wavelength of 173 $\mu$m, primarily agreeing with the spacing of the solidified ripples in Fig. 11(a). The enlargement of this dimple surface shows broken and distorted lamellar eutectics radiating from the ripples center, as shown in Fig. 11(b), which is apparently a nucleation site. A detailed study of these broken and distorted lamellar eutectics [Fig. 11(c)] shows a morphology similar to that formed inside the samples [Fig. 8(c)]. These broken lamellas are also analo-

gous with the anomalous eutectics formed under rapid solidification conditions [16] in respect of morphology.

According to Danilov's theory [31], there are two modes of the capillary wave induced by an external acoustic field on the surface of the flattened drops. When $k_c h/2 \geqslant 1$, where $h$ is the thickness of the flattened drop, the frequencies of the symmetric and antisymmetric waves are the same and equal to half of the acoustic frequency (Faraday effect). This condition is satisfied in the present experiment ($k_c h/2 \approx 18$). Considering that the drop is in a cylindrical symmetry, and the amplitudes of the two modes are the same on the drop surface in the present case, the displacement of the capillary wave can be expressed as

$$\eta = \eta_0 \exp(\kappa t)\exp(-j\omega_c t)\sinh(k_c z) J_0(k_c r), \qquad (16)$$

where $\eta$ is the displacement of the capillary wave, $r$ is the radial position on the drop surface, $z$ is the vertical position with $z=0$ being the equator plane of the drop, $J_0$ is the Bessel function of order 0, and $\eta_0$ is a coefficient determined by the initial condition. Here,

$$\kappa = \frac{P k_c}{4\rho_s h \omega_c} - 2\nu_s k_c^2 \qquad (17)$$

in which, $P$ is the pressure amplitude exerted on the drop surface and $\nu_s = 1.76\times 10^{-7}$ m$^2$/s$^2$ is the viscosity of the liquid sample. If $P$ exceeds a critical value of $P_c = 8\nu_s \rho_s k_c h \omega_c$, $\kappa$ will be positive, and the excitation overcomes damping and the capillary wave grows. This threshold pressure gives a critical acceleration of $a_c = 4\nu_s k_c \omega_c$, which is estimated to be $1.3\times 10^3$ m/s$^2$ at the present experiment and is of the same order as that predicted by Eq. (14). Therefore, it is reasonable that the capillary ripples are excited by the forced surface vibration of the flattened drop. Moreover, it should be noticed in Eq. (14) that the distribution of the surface vibration amplitude takes the form of $(1 - r^2/R^2)^{1/2}$. It means that the surface vibration is most intense at the center of the sample disk. Thereby, it is easy to understand that the capillary ripples originate from the central part of the sample disk.

Once the capillary ripples are excited, they grow exponentially into instability or are dumped out by the viscosity of the liquid drop. In the former case, there appears a large pressure perturbation in the thin layer of the drop surface, which may further generate cavitation if there are preexistence gas microbubbles. It is well known that the cavitation effect produces transient ultrahigh pressure (which can be up to 5 GPa [47]) after the collapse of the microbubble and initiates nucleation in the undercooled liquid by raising the local melting temperature and lowering the local activity energy for nucleation [24]. The rise of melting temperature can be expressed by: $\delta T_M = (T_M \Delta V/\Delta H)(P - P_0)$, where, $T_M = 456$ K is the melting temperature at atmospheric pressure, $P_0$. $\Delta V = 6.7\times 10^{-6}$ m$^3$/mol and $\Delta H = 7280$ J/mol are the volume change and enthalpy change due to liquid-solid transformation, respectively. For a high pressure of 1 GPa, the local melting temperature of Pb-Sn eutectic alloy will be elevated by 42 K, which makes the undercooling level and nucleation probability at the vicinity of the cavitation site much higher than that in the bulk melt. The initial pressure distribution of the capillary wave is plotted in Fig. 12 by assuming the pressure amplitude to be the critical pressure $P_c = 2.28\times 10^4$ Pa. It is obvious that the cavitation is more likely to take place at the center of the drop disk surface. Therefore, it is not surprising that both the capillary waves and the nucleation originate from the same site.

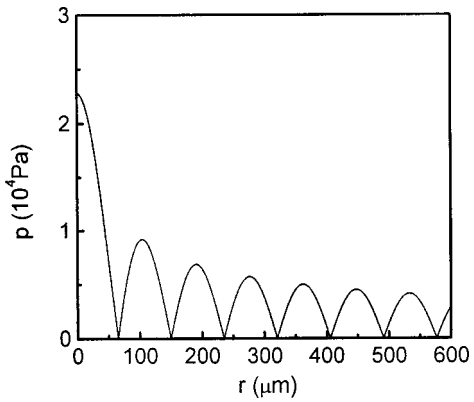


FIG. 12. Pressure amplitude distribution of the capillary wave on the drop surface.

## V. CONCLUSIONS

The containerless melting and solidification of Pb-Sn eutectic alloy samples with a high density of $8.5\times 10^3$ kg/m$^3$ have been successfully accomplished by applying a single-axis acoustic levitation method. The physical conditions for stabile levitation during heating and cooling are analyzed, which are strongly affected by the temperature variation and should be carefully controlled during the experiment. The molten Pb-Sn eutectic drops are highly undercooled by up to 38 K, far beyond the coupled zone for eutectic growth, which results in a microstructural transition from lamellar eutectics to dendrites of (Pb) and (Sn) phases as the undercooling increases. Compared with the common static conditions, some additional characteristics are observed in the microstructures of acoustically levitated samples: the breaking of the eutectic lamellas, suppression of gravity-induced macrosegregation of (Pb) and (Sn) dendrites, and heterogeneous nucleation related to capillary ripples on the sample surface. The broken lamellas and reduction of gravity-induced macrosegregation may be attributed to the complicated internal flow inside the levitated drop, jointly induced by shape oscillation, bulk vibration, and rotation of this drop. The spreading ripples on the sample surface are believed to be capillary waves excited by forced surface vibration and the origin of the capillary waves is also found to be a potent nucleation site.

## ACKNOWLEDGMENTS

This work was supported by the National Natural Science Foundation of China under Grants Nos. 50221101, 50101010, and 50271058, Huo Yingdong Education Foundation under Grant No. 71044, and the Doctorate Foundation of Northwestern Polytechnical University.

[1] C. D. Rosa, C. Park, E. L. Thomas, and B. Lotz, Nature (London) **405**, 433 (2000).
[2] F. Droplet, K. R. Elder, M. Grant, and J. M. Kosterlitz, Phys. Rev. E **61**, 6705 (2000).
[3] M. Plapp and A. Karma, Phys. Rev. E **60**, 6865 (2000).
[4] M. Ginibre, S. Akamatsu, and G. Faivre, Phys. Rev. E **56**, 780 (1997).
[5] K. R. Elder, J. D. Gunton, and M. Grant, Phys. Rev. E **54**, 6476 (1996).
[6] K. Kassner, C. Misbah, and R. Baumann, Phys. Rev. E **51**, R2751 (1995).
[7] C. Misbah and D. E. Temkin, Phys. Rev. E **49**, 3159 (1994).
[8] Karma, Phys. Rev. E **49**, 2245 (1994).
[9] Valance, C. Misbah, D. Temkin, and K. Kassner, Phys. Rev. E **48**, 1924 (1993).
[10] K. Kassner and C. Misbah, Phys. Rev. Lett. **66**, 445 (1991).
[11] K. A. Jackson and J. D. Hunt, Trans. Metall. Soc. AIME **236**, 1129 (1966).
[12] W. Kurz and D. J. Fisher, *Fundamentals of Solidification*, 4th Ed. (Trans Tech, Switzerland, 1998), Chap. 5, p. 93.
[13] E. H. Brandt, Nature (London) **413**, 474 (2001).
[14] J. K. R. Weber, J. J. Felten, B. Cho, and P. C. Nordine, Nature (London) **393**, 769 (1998).
[15] R. Willnecker, D. M. Herlach, and B. Feuerbacher, Phys. Rev. Lett. **62**, 2707 (1989).
[16] B. Wei, D. M. Herlach, and F. Sommer, J. Mater. Sci. Lett. **12**, 1774 (1993).
[17] E. H. Brandt, Science **243**, 349 (1989).
[18] S. Bauerecker and B. Neidhart, J. Chem. Phys. **109**, 3709 (1998).
[19] T. Volkman, G. Wilde, R. Willnecker, and D. M. Herlach, J. Appl. Phys. **83**, 3028 (1998).
[20] W. K. Rhim, K. Ohsaka, and P. F. Paradis, Rev. Sci. Instrum. **70**, 2796 (1999).
[21] M. V. Berry and A. K. Geim, Eur. J. Phys. **18**, 307 (1997).
[22] A. K. Geim, M. D. Simon, M. I. Boamfa, and L. Q. Heflinger, Nature (London) **400**, 323 (1999).
[23] K. Ohsaka and E. H. Trinh, J. Cryst. Growth **96**, 973 (1989).
[24] K. Ohsaka, E. H. Trinh, and M. E. Glicksman, J. Cryst. Growth **106**, 191 (1990).
[25] A. Biswas, J. Cryst. Growth **147**, 155 (1995).
[26] W. J. Xie and B. Wei, Chin. Phys. Lett. **18**, 68 (2001).
[27] W. J. Xie and B. Wei, Appl. Phys. Lett. **79**, 881 (2001).
[28] W. J. Xie and B. Wei, Phys. Rev. E **66**, 026605 (2002).
[29] L. V. King, Proc. R. Soc. London, Ser. A **147**, 212 (1934).
[30] L. P. Gor'kov, Sov. Phys. Dokl. **6**, 773 (1962).
[31] S. D. Danilov and M. A. Mironov, J. Acoust. Soc. Am. **92**, 2747 (1992).
[32] P. Collas, M. Barmatz, and C. Shipley, J. Acoust. Soc. Am. **86**, 777 (1989).
[33] R. Trivedi, P. Magnin, and W. Kurz, Acta Metall. **35**, 971 (1987).
[34] J. Lipton, W. Kurz, and R. Trivedi, Acta Metall. **35**, 957 (1987).
[35] H. C. deGroh and V. Laxmannan, Metall. Trans. A **19A**, 2651 (1988).
[36] H. J. Fecht and J. H. Perepezko, Metall. Trans. A **20A**, 787 (1989).
[37] R. G. Holt and E. H. Trinh, Phys. Rev. Lett. **77**, 1274 (1996).
[38] C. P. Lee, A. V. Anilkumar, and T. G. Wang, Phys. Fluids A **3**, 2497 (1991).
[39] E. H. Trinh, P. L. Marston, and J. L. Robey, J. Colloid Interface Sci. **124**, 95 (1988).
[40] A. V. Anilkumar, C. P. Lee, and T. G. Wang, Phys. Fluids A **5**, 2763 (1993).
[41] T. G. Wang, E. H. Trinh, A. P. Croonquist, and D. D. Elleman, Phys. Rev. Lett. **56**, 452 (1986).
[42] B. Wei, Acta Metall. Mater **40**, 2739 (1992).
[43] X. F. Shen, A. V. Anilkumar, R. N. Grugel, and T. G. Wang, J. Cryst. Growth **165**, 438 (1996).
[44] A. V. Anilkumar, R. N. Grugel, X. F. Shen, and T. G. Wang, J. Appl. Phys. **73**, 4165 (1993).
[45] E. V. Zharikov, L. V. Prihod'ko, and N. R. Storozhev, J. Cryst. Growth **99**, 910 (1990).
[46] D. V. Lyubimov, T. P. Lyubimova, S. Meraji, and B. Roux, J. Cryst. Growth **180**, 648 (1997).
[47] R. Hicking, Phys. Rev. Lett. **73**, 2853 (1994).